# Computational Design of Non-Equiatomic CoCrFeNi Alloys Towards Optimized Mechanical and Surface Properties

Zhengyu Zhang<sup>a</sup>, Yi Yao<sup>b</sup>, Liping Liu<sup>c</sup>, Tianyou Mou<sup>c</sup>, Hongliang Xin<sup>c,\*</sup>, Lin Li<sup>b</sup>, and Wenjun Cai<sup>a,\*</sup>

- a. Department of Materials Science and Engineering, Virginia Polytechnic Institute and State University, Virginia, 24061, United States
- b. Department of Metallurgical and Materials Engineering, The University of Alabama, Tuscaloosa, AL, 36487, United States
- c. Department of Chemical Engineering, Virginia Polytechnic Institute and State University, Virginia, 24061, United States
- \* Corresponding author email addresses: <a href="https://hxin.org/hxin.org/hxin.org/">hxin@vt.edu</a> (H. Xin), <a href="mailto:caiw@vt.edu">caiw@vt.edu</a> (W. Cai).

#### **Abstract**

Multi-principal element alloys (MPEAs), also known as high entropy alloys, are often designed to be equiatomic from entropy considerations. We show that relaxing such constraint could lead to enhanced mechanical and surface properties, which is critical for applications of MPEAs under complex environment where both stress and corrosion attacks occur. Specifically, using spin-polarized density functional theory calculations, the effects of chromium (Cr) concentration on the mechanical and surface properties of CoCrFeNi with  $\sim$  16, 25, and 34 at.% Cr were studied. It was found that Cr plays significant roles in affecting both mechanical properties and surface reactivity. Alloys with higher Cr percentage showed higher Young's modulus and Poisson's ratio, as well as higher chemical activity of surface Cr atoms. Overall, a non-equiatomic composition of  $Co_{22}Cr_{34}Fe_{22}Ni_{22}$  was predicted with simultaneously optimized strength and surface reactivity.

#### **Kev words:**

Multi-principal element alloys, High entropy alloys, CoCrFeNi alloys, Density functional theory, Electron work function, Mechanical properties, Surface reactivity

#### 1. Introduction

Multi-principal element alloys (MPEAs), also known as high entropy alloys, are often composed of four or more principal elements with equal concentrations, distinct from conventional metals with typically one principal element 1-3. MPEAs are attracting increasing research interest lately due to their outstanding thermal, mechanical, and corrosion properties <sup>4-12</sup>, especially promising as the next-generation structural materials for applications under complex environments <sup>2, 13-15</sup>. While current research on MPEAs often focuses on optimizing one type of material property, especially mechanical properties (including strength, ductility, toughness and creep resistance) 3, 16-18, little work has been done in designing alloys with simultaneously optimized mechanical and surface properties such as corrosion resistance 19-23, which is essential for future application of MPEAs in offshore infrastructure, transformation, aerospace, energy and biomedical industries where both stress and corrosive environment are present. In this work, we present a computational study towards the development of strong and corrosion-resistant MPEAs by calculating composition-dependent mechanical properties (i.e. elastic constants) and surface reactivity (e.g. electron work function and density of electronic states), to identify an optimum alloy composition that might differ from the commonly studied equiatomic composition from only entropy considerations <sup>24, 25</sup>. As shown later, there exists a complex compositional-depednece of the mechanical and surface properties of MPEAs, and the identified optimum composition indeed has better characteristics than the equiatomic composition.

In this study, we focus on CoCrFeNi alloys, a family of widely studied MPEAs with high thermal stability and simple crystal structure (i.e. face-centered cubic solid solution), which have also been used as a base system for a variety of other MPEAs <sup>26-28</sup>. Past research shows that the cocktail effects of MPEAs leads to a complex composition-structure-property relationship, further challenging the design of strong and corrosion-resistant MPEAs. For example. Wu et al. <sup>29</sup> and Gludovatz et al. <sup>30</sup> showed that the nature of the constituent elements. rather than the number of principal elements, is important for the mechanical properties and damage tolerance of CoCrFeNi-based MPEAs. For example, Wu et al. <sup>29</sup> showed that both the strength and ductility of NiCoCr is higher than those of FeNiCoCrMn (aka cantor alloy), as well as various other four-element MPEAs (e.g. FeNiCoCr, FeNiCoMn, NiCoCrMn). In this alloy system, Cr was identified to be the most potent strengthner, whose addition increases the stacking fault energy of the alloy and promote martensitic transformation instead of deformation twinning 29. In terms of surface reactivity such as corrosion and oxidation resistance, much fewer studies have been reported for this system to date as compared to those on mechanical properties. Koga et al. <sup>21</sup> showed that Cr-rich (25 - 45 at.% Cr) CrCoNi alloys exhibit high corrosion resistance in simulated seawater, outperforming conventional austenitic stainless steels and Ni-based superalloys. Kim et al. 31 demonstrated that high-temperature

oxidation behavior of CrCoFeNiMn MPEAs is largely affected by Cr and Mn elements due to their dominance in surface oxidation. Gao et al. <sup>32</sup> showed that Cr is a highly reactive element on the surface of CrMnFeCoNi and CrFeCoNiPd MPEAs, leading to the formation of spinel MnCr<sub>2</sub>O<sub>4</sub> oxide scale at the presence of Mn and the formation of rutile CrO<sub>2</sub> when Mn is replaced by non-reactive Pd in the alloy. All together, these past research highlights the great potential of tuning Cr-content in MPEAs to simultaneously tailor their mechanical and surface properties.

The goal of this research is to study the effects of Cr concentration on the mechanical and surface properties of CoCrFeNi system and establish a composition-property relationship. The Cr content of the alloy was varied, while the other principal elements (i.e. Co, Fe, and Ni) were kept equiatomic. For mechanical properties, the Young's modulus (E), Bulk modulus (B), Shear modulus (G), Poisson's ratio (v), and B/G ratio were calculated. For surface chemical stability, the electron work function (EWF) of the alloys was calculated. EWF is the minimum energy required to extract an electron from a solid at Fermi level to a point in vacuum. EWF reflects the difficulty of changing electronic states and has been found to correlate with corrosion resistance experimentally <sup>33-35</sup>. Typically, given a similar microstructure, a higher EWF contributes to a more stable electronic state and better corrosion resistance <sup>36</sup>. For example, Luo et al. <sup>36</sup> showed that EWF carries the information on the surface electron behavior and overall corrosion properties of multiphase low-carbon steel. They found that alloys with higher EWFs exhibit higher mechanical strength and larger resistance to corrosion due to stronger overall confinement to electrons and stronger bonding stability. Wang et al. <sup>37</sup> studied the corrosion behavior of CoCrFeMnNi high entropy alloy films experimentally, and found that the ones with surfaces with higher EWF is more hydrophobic and corrosion resistant in 3.5 wt.% NaCl solutions. Hasannaeimi et al. 38 showd that in multiphase AlCoCrFeNi high entropy alloys consisting of eutectic B2 and L1<sub>2</sub> phases, the L1<sub>2</sub> phase was more corrosion resistant locally due to its higher EWF. Nonetheless, it should be pointed out that deviation from this general trend has also been reported, such as in Ti-Zr-Be-(Ni-Fe) metallic glasses <sup>39</sup>, highlighting the challenges in correlating microstructure, surface chemistry and corrosion behaviours, especially for alloys with complex disordered structure and multiple consitituing elements. We also note here that EWF is used as a general indicator for surface chemical reactivity here, while the calculations of more specific corrosion or electrochemical parameters such as electrode potential, hydroxyl and oxygen adsorption energies etc. 40-42 requires consideration of the specific corrosive environment of interest (e.g. aquesous, high temperature, hydrogen-containing, liquid metal environment), and thus are beyond the scope of the current work.

.

#### 2. Results and Discussion

#### 2.1. Structure and lattice constant

Three alloy compositions were studied using Vienna *ab initio* simulation package (VASP): Co<sub>28</sub>Cr<sub>16</sub>Fe<sub>28</sub>Ni<sub>28</sub>, Co<sub>25</sub>Cr<sub>25</sub>Fe<sub>25</sub>Ni<sub>25</sub>, Co<sub>22</sub>Cr<sub>34</sub>Fe<sub>22</sub>Ni<sub>22</sub>, where the Cr percentage was varied from ~16 at.%, 25 at.%, and 34 at.%, while the other elements remain in equal concentrations. These alloys are referred as Cr16, Cr25, and Cr34 for simplicity hereafter. See calculation details in Section 4. Fig. 1 shows the constructed special quasirandom structure (SQS) cell and the calculated total energy as a function of the lattice constant. Table 1 lists the equilibrium lattice constant (*d*), which was calculated from the lowest energy point. It can be seen that *d* increases slightly with Cr%, from 3.56 Å for Cr16 to 3.53 Å for Cr34 alloy. Among all principal elements, Cr has a relatively large atomic size of 1.40 Å, as compared to Ni (1.35 Å), Fe (1.40 Å), and Co (1.35 Å), thus the change in *d* contradicts the rule of mixture (ROM) <sup>43, 44</sup>. In addition, the calculated results of Cr25 alloy (3.54 Å) are in good agreement with previous reports from DFT calculations (e.g. 3.547 Å from Ref <sup>45</sup> and 3.534 Å from Ref <sup>46</sup>), as well as prior experimental measurements (3.559 Å from Ref <sup>47</sup>).

### 2.2. Magnetic properties

One important consideration of the calculation is the paramagnetic or ferromagnetic properties of the principal element Fe, Co, and Ni <sup>48-51</sup>, which cannot be neglected for alloys containing 50% or more magnetic elements <sup>52, 53</sup>. As reported by Guan et al., antiferromagnetic elements like Cr plays an important role in the total average magnetic moment and can affect defect formation of CoCrNi-based alloys 54. Lu et al. found that the interfacial energy was greatly affected by magnetic effects at the Ni (111)/Cr (110) interface 55. In general, more magnetic elements will lead to higher magnetization <sup>56, 57</sup>, and consequently affecting the precision of mechanical properties calculation. In this work, the spin-polarized calculation was applied to account for the magnetic effects of all elements in the alloy, which was found to greatly improve the accuracy of calculated properties, as detailed afterwards. Fig. 2 and Table S1 (Supplemental Materials) summarizes the calculated magnetic property results. In the literature, spin-polarization was sometimes neglected with relatively large cell in DFT, because it is time-consuming to compute, and it was argued that Cr has a reduction effect on magnetism when paired with Co/Fe/Ni 55. However, energy is indeed varied between the results with or without the spin-polarized method, as shown in both previous work <sup>58</sup> and our results (presented later in Table 2). Fig. 2 shows that Cr of all alloys exhibit negative magnetic moment and shows a reduction effect on magnetism. With more Cr content in the alloy, the total average magnetic moment of Cr16, Cr25 and Cr34 decreases from 0.99 µ<sub>B</sub> to 0.41 µ<sub>B</sub>. Comparing our results with previously reported first principle calculations <sup>59</sup>, it can be seen that though the magnetic moment of Cr changes when other element is added into the CoCrFeNi base alloy, it is always the lowest among all. We argue that since mechanical calculations using the energy-strain method <sup>60</sup> are highly sensitive to the accuracy of energy calculation, it is important that magnetic effects are included in the DFT calculation. To compensate for the high computational cost due to the complicated structure of the CoCrFeNi system, here we included spin-polarized calculation in our large CoCrFeNi system with relatively lower k-points and energy cut-off.

# 2.3. Mechanical properties

The mechanical properties were calculated using the spin-polarized method discussed above, and found to be in great agreement with previous experimental results  $^{61}$ , especially for the shear and Young's modulus, as shown in **Table S1** (Supplemental Materials) for all the alloys and **Table 2** for Cr25 alloy. Specifically, **Table 2** shows that the calculated elastic constants were overestimated without spin-polarization. For example, when using the same k-points and energy cutoff, Young's modulus (E) of 387 GPa was calculated for Cr25 without spin-polarization, vs. 226 GPa with it, the latter of which agrees much better with the experiments (214 GPa, room temperature  $^{61}$ ). A higher k-points of  $7 \times 7 \times 7$  and energy cutoff 450 eV without spin-polarization was applied for comparison, which gave a B/G ratio 2.18, greatly deviating from experiment observation (B/G = 1.65) and calculated results using spin-polarization (B/G = 1.75).

Fig. 3(a) summarizes the calculated modulus of all samples and Fig. 3(b) summarizes the B/G ratio and Poisson's ratio (υ), which can be related to the propensity for ductility and formability of the material <sup>62, 63</sup>. For example, a B/G ratio of 1.75 was found to be a critical value, above which, materials tend to have ductile instead of brittle behavior <sup>62, 63</sup>. Poisson's ratio (υ), on the other hand, is used as another criterion for ductility, as it reflects material's stability against shear stress and higher Poisson's ratio often means better formability <sup>64</sup>. Interestingly, alloy Cr25 exhibited the highest E and G, yet the smallest B of all samples, resulting in the lowest B/G ratio of 1.75. In addition, this equiatomic compositional alloy also shows the smallest υ. On the other hand, Cr34 alloy shows the highest B (181.804 GPa) and highest B/G ratio (2.096) of all samples. In all three compositions, Cr25 alloy shows the highest while Cr16 shows the lowest stiffness; Cr34 alloy shows the largest while Cr25 shows the smallest ductility. Considering both properties, Cr34 is identified to be an optimum composition for both high stiffness and propensity for ductility. It is also interesting to note that the predicted trend of υ and B/G as a function of composition differs from the ROM calculations, as shown in Table 3.

#### 2.4. Surface reactivity analysis

The surface reactivity of all samples is evaluated via EWF calculations, which provides a measurement of surface chemical stability against reactions such as corrosion and oxidation 65. As dissussed in the introduction, and also pointed out by Wang et al. 66 and Huang et al. 67, alloys (e.g. CoCrFeNi-based alloy) with a higher EWF tend to exhibit a higher corrosion resistance. **Table 1** and **Fig. 4** summarize EWF of (100), (110), and (111) surfaces of the three alloys. In all materials, (111) surfaces show the highest EWF, while (110) surfaces exhibit the lowest EWF, indicating that the later is the most chemically active. In terms of the compositional effect, examining the easiest reactive plane (110), the EWF was found to increase monotonically with Cr%, from 4.164 eV for Cr16 to 4.181 eV for Cr34. This trend can not be simply estimated from the ROM predictions of the constituting elements, as shown in **Table 3**. Note that such a ROM rule was found previously to work well for binary Cu-Ni solid solutions from prior experimental study 67. Such observations further highlights the necessity of different design rules for MPEAs than that of traditional alloys.

To further understand the effects of Cr percentage on the surface reactivity, density of states (DOS) and d-band center were calculated, which were often related to surface chemical activity such as reaction and adsorption in a corrosive environment <sup>68, 69</sup>. For example, the surface chemical reactivity of transition-metals has been often understood in terms of the adsorption of environmental atoms and molecules onto metal surfaces via the d-band model 70, which indicates a scaling relationship between atom/molecule adsorption energy and the dband center, and successfully confirmed by a series of X-ray spectroscopy experiments 71. For example, the O adsorption energies increase (i.e. the absolute values decrease) for Au and Pt surfaces as the d-band center shifts in the negative direction <sup>70</sup>. Typically, a negative adsorption energy indicates that the adsorption was thermopositive and a large absolute value of adsorption energy indicates more stable adsorption 72,73. Alloying can be a strategy to tailor d-band center of metals <sup>74</sup>, and it is indeed observed from our calculations. Density of states (DOS), oxidation state and d-band center of Cr on (110) surfaces are shown in Fig. 5, and the total and partial DOS of all the constituting elements are shown in Fig. S1 (Supplemental Materials). Fig. 5(a) shows the normalized partial density of state (PDOS) of Cr in Cr16, Cr25 and Cr34, where E- $E_f = 0$  eV represents the Fermi level. It can be seen that with increasing Cr contant in the sample (from Cr16 to Cr34), the d-band center of Cr moved further away from the Fermi level, suggesting an increase in Cr chemical stability 75. From Fig. S1 and the d-band center results in Table 4, it can be seen that Co, Fe and Ni all have negative center position and are not sensitive to the composition change, whereas the Cr d-band center decreases monotonically from -0.08 eV in Cr16 to -0.39 eV in Cr34, as plotted in Fig. 5(b). Such surface states indicates that Cr is the preferred adsorption site for environmental atoms/molecules (e.g. oxygen and water), and the most reactive sample is Cr16 while the least reactive is Cr34 alloy. This trend also agrees with the Richardson-Ellingham diagram, where the oxidation of Cr has the smallest Gibbs free energy in all oxidation reactions of principal elements <sup>76</sup>. This behavior is also consistent with previous X-ray spectroscopy characterization of the native oxide and passive films of CoCrFeMnNi 77, where Cr (hydr)oxide were found to be dominant, followed by Fe, Mn, and Co oxides. Preliminary calculations of Pourbaix diagram (Supplemental Materials Fig. S2) of these three alloys also confirms the dominant roles of Cr in the formation of oxides such as Cr<sub>2</sub>O<sub>3</sub>, CoCr<sub>2</sub>O<sub>4</sub>, FeCr<sub>2</sub>O<sub>4</sub> in neutral to basic water. In terms of oxidation state, we note that the Bader charge of Cr is +1.51 in CrO<sub>2</sub>, which corresponds to the +4 oxidation state. Linear interpolation was adoped to estimate the Cr oxidation state using the Bader charge of alloys and CrO<sub>2</sub>. Cr in Cr34 is found to be less oxidized and exhibits higher reducibility in oxidizing environments. Prior experimental study 78 on the passive layer of CoCrFeNi indicated that higher Cr concentration enhanced the passive layer stability. According to these results, Cr34 composition, rather than the equiatomic composition of Cr25, is predicted to be more corrosionresistant. These results also indicate that the local environment of Cr, e.g. which are its neighboring atoms, greatly affect its chemical reactivity. Summarizing the alloying effects on surface chemical reactivity, the calculated results thus suggest that the Cr\%, rather than the other elements, is the most important for corrosion resistance. Finally, the compositionmechanical-surface property relationships are summarized in Fig. 6. Overall, C34 composition is predicted to the optimum, which exhibited the highest ductility (as indicated by B/G and Poisson's ratio), relatively high Young's modulus, and the highest EWF among all compositions studied here.

#### 3. Conclusions

In summary, we found that Cr content greatly affected both mechanical and surface chemical properties of CoCrFeNi MPEAs. Young's modulus and ductility (as indicated by B/G and Poisson's ratio) were higher in alloys with larger Cr percentage, and EWF increased monotonically with Cr percentage. Additionally, Cr was found to be the preferred reaction site while the surface reactivity decreased with increasing Cr content, indicating an increase of corrosion resistance. Towards the design goal of achieving high strength and corrosion resistance, Cr34 is thus predicted to be the optimum composition among those studied. Computationally, we found the use of spin-polarization method is necessary for calculating CoCrFeNi properties with good accuracy. The addition of spin-polarization often requires a balance between other calculation parameters, such as unit cell, cut-off energy, and k-points.

#### 4. Methods

#### 4.1. DFT calculations

Vienna *ab initio* simulation package (VASP) <sup>79,80</sup> and projected augmented plane-wave (PAW) implementation were used for all calculations. Structure optimization was performed

using the Perdew-Burke-Ernzerhof (PBE) version of the generalized gradient approximation (GGA) of the exchange-correlation functional <sup>81</sup>, with an energy cutoff 400 eV for the planewave basis set. The supercell structure was relaxed until the Hellmann-Feynman forces on each atom was less than 0.03 eV/Å and an energy convergence criterion of 10<sup>-5</sup> eV was used. Special quasirandom structure (SQS) method proposed by Zunger et al. <sup>82</sup> was used in this work to create periodic random alloy cells of CoCrFeNi via the alloy theoretic automated toolkit (ATAT) package <sup>83</sup>.

#### 4.2. Mechanical properties calculations

Mechanical properties were calculated over a 32-atom cell with  $4\times4\times4$  Monkhorst-Pack mesh of k-points using the energy-strain method  $^{60, 84}$ , which is based on the energy variation upon the application of a small elastic strain to the equilibrium lattice. The elastic stiffness tensor was calculated from the second-order derivative of the total energy vs. strain. This method requires less computational cost to achieve the same accuracy than the stress-strain method  $^{60, 84}$ . From the calculated elastic stiffness tensor [ $c_{ij}$ ], the projection method was then applied to calculate the elastic constants [ $C_{ij}$ ] using the equations below  $^{85, 86}$ :

$$C_{11} = \frac{1}{3}(c_{11} + c_{22} + c_{33}), \tag{1}$$

$$C_{12} = \frac{1}{3}(c_{12} + c_{13} + c_{23}), \tag{2}$$

and

$$C_{44} = \frac{1}{3}(c_{44} + c_{55} + c_{66}). \tag{3}$$

The calculated elastic constants satisfied the following machenical stability criteria 87:

$$C_{11} - C_{12} > 0, (4)$$

$$C_{11} + 2C_{12} > 0, (5)$$

and

$$C_{44} > 0.$$
 (6)

Voigt-Reuss approximation was used in the calculation, based on the assumption of uniform strain and uniform stress throughout the crystal  $^{88,89}$ . The elastic stiffness (flexibility) matrix  $S_{ij}$  can be given as the inverse of the elastic stiffness matrix  $C_{ij}$  as  $[S_{ij}] = [C_{ij}]^{-1}$ . Voigt bulk modulus  $(B_V)$  and shear modulus  $(G_V)$  are given by:

$$B_{v} = \frac{1}{3}(C_{11} + 2C_{12}), \tag{7}$$

and

$$G_{V} = \frac{1}{5}(C_{11} - C_{12} + 3C_{44}). \tag{8}$$

Reuss bulk modulus (B<sub>r</sub>) and shear modulus (G<sub>r</sub>) are given by

$$B_{\rm r} = \frac{1}{3S_{11} + 6S_{12}},\tag{9}$$

and

$$G_{\rm r} = \frac{15}{4S_{11} - 4S_{12} + 3S_{44}}. (10)$$

Hill's average for shear (G) and bulk modulus (B), Young's modulus (E), Poisson's ratio (υ) are given by <sup>90</sup>:

$$B = \frac{1}{2}(B_r + B_v), \tag{11}$$

$$G = \frac{1}{2}(G_r + G_v), \tag{12}$$

$$E = \frac{9BG}{3B+G},\tag{13}$$

and

$$v = \frac{3B - E}{6B}.\tag{14}$$

# 4.3. Surface properties calculations

A cell of 256 atoms with a  $(1\times1\times1)$  k-point mesh with spin-polarized method was used for the surface EWF and density of state calculations. The cell size is larger than those used for the mechanical property calculation because EWF is a surface property, which can be better presented by larger SQS structure and larger surface areas. Three orientations of (100), (110) and (111) planes were cut for calculation for the Cr16, 25, and 34 alloys, as defined earlier. The EWF refers to the energy required to move an electron from the surface of the material to an infinite distance away  $^{91}$ . In our calculations, the EWF is given as  $\phi = E_{vac} - E_F = \phi_0 + \Delta \phi_{dipole}$ , where  $E_{vac}$  and  $E_F$  is the calculated Vacuum and Fermi level energy respectively, as shown in Fig. 10 of Ref.  $^{72}$ .  $\phi_0$  is the intrinsic work function of the surface without dipole, and  $\Delta \phi_{dipole}$  is the change of work function from surface dipole. The origin of  $\Delta \phi_{dipole}$  is of electrostatic nature and is given by the solution of the Helmholtz-equation  $^{92, 93}$ . Specifically, after applying dipole correlation, the difference between the potential energy of the Vacuum and Fermi level was used to calculate the EWF.

# Data availbility

Data are available upon reasonable request from the corresponding author.

#### **Code availbility**

Code are available upon reasonable request from the corresponding author.

# Competing interests' statement

The Authors declare no Competing Financial or Non-Financial Interests.

# Acknowledgement

The authors gratefully acknowledge funding provided by US National Science Foundation (DMR-2104655/2104656). The computational resource used in this work is provided by the advanced research computing (ARC) at Virginia Polytechnic Institute and State University.

## References

- 1. J.W. Yeh, S.K. Chen, S.J. Lin, J.Y. Gan, T.S. Chin, T.T. Shun, C.H. Tsau and S.Y. Chang: Nanostructured High-Entropy Alloys with Multiple Principal Elements: Novel Alloy Design Concepts and Outcomes *Advanced Engineering Materials*. **6**(5), 299 (2004).
- 2. D.B. Miracle and O.N. Senkov: A critical review of high entropy alloys and related concepts *Acta Mater.* **122**, 448 (2017).
- 3. E.P. George, W.A. Curtin and C.C. Tasan: High entropy alloys: A focused review of mechanical properties and deformation mechanisms *Acta Mater.* **188**, 435 (2020).
- 4. S.Q. Xia, M.C. Gao and Y. Zhang: Abnormal temperature dependence of impact toughness in Al CoCrFeNi system high entropy alloys *Materials Chemistry and Physics.* **210**, 213 (2018).
- 5. W.H. Liu, J.Y. He, H.L. Huang, H. Wang, Z.P. Lu and C.T. Liu: Effects of Nb additions on the microstructure and mechanical property of CoCrFeNi high-entropy alloys *Intermetallics*. **60**, 1 (2015).
- 6. H. Jiang, K. Han, D. Qiao, Y. Lu, Z. Cao and T. Li: Effects of Ta addition on the microstructures and mechanical properties of CoCrFeNi high entropy alloy *Materials Chemistry and Physics*. **210**, 43 (2018).
- 7. W.H. Liu, Z.P. Lu, J.Y. He, J.H. Luan, Z.J. Wang, B. Liu, Y. Liu, M.W. Chen and C.T. Liu: Ductile CoCrFeNiMox high entropy alloys strengthened by hard intermetallic phases *Acta Materialia*. **116**, 332 (2016).
- 8. W.-R. Wang, W.-L. Wang, S.-C. Wang, Y.-C. Tsai, C.-H. Lai and J.-W. Yeh: Effects of Al addition on the microstructure and mechanical property of AlxCoCrFeNi high-entropy alloys *Intermetallics.* **26**, 44 (2012).
- 9. T.-T. Shun, L.-Y. Chang and M.-H. Shiu: Microstructure and mechanical properties of multiprincipal component CoCrFeNiMox alloys *Materials Characterization*. **70**, 63 (2012).
- 10. Y.Z. Shi, B. Yang and P.K. Liaw: Corrosion-Resistant High-Entropy Alloys: A Review *Metals-Basel*. **7**(2), (2017).
- 11. H.X. Cheng, Z.M. Pan, Y. Fu, X.F. Wang, Y. Wei, H. Luo and X.G. Li: Review-Corrosion-Resistant High-Entropy Alloy Coatings: A Review *J Electrochem Soc.* **168**(11), (2021).
- 12. N. Birbilis, S. Choudhary, J.R. Scully and M.L. Taheri: A perspective on corrosion of multiprincipal element alloys *Npj Mat Degrad*. **5**(1), (2021).
- 13. Y. Zhang, T.T. Zuo, Z. Tang, M.C. Gao, K.A. Dahmen, P.K. Liaw and Z.P. Lu: Microstructures and properties of high-entropy alloys *Progress in Materials Science*. **61**, 1 (2014).
- Z. Niu, J. Xu, T. Wang, N. Wang, Z. Han and Y. Wang: Microstructure, mechanical properties and corrosion resistance of CoCrFeNiWx (x = 0, 0.2, 0.5) high entropy alloys *Intermetallics*. 112, 106550 (2019).
- 15. W.R. Zhang, P.K. Liaw and Y. Zhang: Science and technology in high-entropy alloys *Sci China Mater.* **61**(1), 2 (2018).
- 16. Z.F. Lei, X.J. Liu, Y. Wu, H. Wang, S.H. Jiang, S.D. Wang, X.D. Hui, Y.D. Wu, B. Gault, P. Kontis, D. Raabe, L. Gu, Q.H. Zhang, H.W. Chen, H.T. Wang, J.B. Liu, K. An, Q.S. Zeng, T.G. Nieh and Z.P. Lu: Enhanced strength and ductility in a high-entropy alloy via ordered oxygen complexes *Nature*. 563(7732), 546 (2018).
- 17. E.P. George, D. Raabe and R.O. Ritchie: High-entropy alloys *Nat Rev Mater.* 4(8), 515 (2019).
- 18. F.G. Coury, C.S. Kiminami, W.J. Botta, C. Bolfarini and M.J. Kaufman: Design and production of Al-Mn-Ce alloys with tailored properties *Mater Design*. **110**, 436 (2016).
- 19. H. Luo, Z.M. Li, A.M. Mingers and D. Raabe: Corrosion behavior of an equiatomic CoCrFeMnNi high-entropy alloy compared with 304 stainless steel in sulfuric acid solution *Corros Sci.* **134**, 131 (2018).
- 20. Y.D. Wu, Y.L. Li, X.L. Liu, Q.J. Wang, X.M. Chen and X.D. Hui: High strength NiMnFeCrAlCu multi-principal-element alloys with marine application perspective *Scripta Mater.* **202**, (2021).
- 21. G.Y. Koga, N. Birbilis, G. Zepon, C.S. Kiminami, W.J. Botta, M. Kaufman, A. Clarke and F.G. Coury: Corrosion resistant and tough multi-principal element Cr-Co-Ni alloys *J Alloy Compd.* **884**, (2021).
- 22. A. Ayyagari, V. Hasannaeimi, H.S. Grewal, H. Arora and S. Mukherjee: Corrosion, Erosion and Wear Behavior of Complex Concentrated Alloys: A Review *Metals-Basel*. **8**(8), (2018).
- 23. X.X. Yu, M.A. Taylor, J.H. Perepezko and L.D. Marks: Competition between thermodynamics, kinetics and growth mode in the early-stage oxidation of an equimolar CoCrFeNi alloy *Acta Mater.* **196**, 651 (2020).

- 24. A.M. Panindre, H.O. Colijn, C.D. Taylor and G.S. Frankel: Microstructure and corrosion of non-equimolar multi-principal element alloys hardened by metastable precipitates *J Alloy Compd.* **894**, (2022).
- 25. T.S. Li, O.J. Swanson, G.S. Frankel, A.Y. Gerard, P. Lu, J.E. Saal and J.R. Scully: Localized corrosion behavior of a single-phase non-equimolar high entropy alloy *Electrochim Acta.* **306**, 71 (2019).
- 26. N.E. Koval, J.I. Juaristi, R.D. Muino and M. Alducin: Structure and properties of CoCrFeNiX multi-principal element alloys from ab initio calculations *Journal of Applied Physics*. **127**(14), (2020).
- 27. Z. Wu, Y.F. Gao and H. Bei: Single crystal plastic behavior of a single-phase, face-center-cubic-structured, equiatomic FeNiCrCo alloy *Scripta Mater.* **109**, 108 (2015).
- 28. S.C. Middleburgh, D.M. King, G.R. Lumpkin, M. Cortie and L. Edwards: Segregation and migration of species in the CrCoFeNi high entropy alloy *J Alloy Compd.* **599**, 179 (2014).
- 29. Z. Wu, H. Bei, G.M. Pharr and E.P. George: Temperature dependence of the mechanical properties of equiatomic solid solution alloys with face-centered cubic crystal structures *Acta Mater.* **81**, 428 (2014).
- 30. B. Gludovatz, A. Hohenwarter, K.V.S. Thurston, H.B. Bei, Z.G. Wu, E.P. George and R.O. Ritchie: Exceptional damage-tolerance of a medium-entropy alloy CrCoNi at cryogenic temperatures *Nat Commun.* 7, (2016).
- 31. Y.K. Kim, Y.A. Joo, H.S. Kim and K.A. Lee: High temperature oxidation behavior of Cr-Mn-Fe-Co-Ni high entropy alloy *Intermetallics*. **98**, 45 (2018).
- 32. J. Gao, J. Ding, Y. Zhang, T. Zhu and Q. Yu: Tuning the near room temperature oxidation behavior of high-entropy alloy nanoparticles *Nano Res.* **15**(4), 3569 (2022).
- 33. A.K. Neufeld, I.S. Cole, A.M. Bond and S.A. Furman: The initiation mechanism of corrosion of zinc by sodium chloride particle deposition *Corrosion Science*. **44**(3), 555 (2002).
- 34. W. Li and D.Y. Li: Influence of surface morphology on corrosion and electronic behavior *Acta Materialia*. **54**(2), 445 (2006).
- 35. X. Huang, H. Lu and D. Li: Understanding the corrosion behavior of isomorphous C• Ni alloy from its electron work function *Materials Chemistry and Physics.* **173**, 238 (2016).
- 36. Y.Z. Luo, Y.Q. Tang, T.F. Chung, C.L. Tai, C.Y. Chen, J.R. Yang and D.Y. Li: Electron work function: an indicative parameter towards a novel material design methodology *Sci Rep-Uk.* 11(1), (2021).
- Z. Wang, D.Y. Li, Y.Y. Yao, Y.L. Kuo and C.H. Hsueh: Wettability, electron work function and corrosion behavior of CoCrFeMnNi high entropy alloy films Surf Coat Tech. 400. (2020).
- 38. V. Hasannaeimi, A.V. Ayyagari, S. Muskeri, R. Salloom and S. Mukherjee: Surface degradation mechanisms in a eutectic high entropy alloy at microstructural length-scales and correlation with phase-specific work function *Npj Mat Degrad.* **3**(1), (2019).
- 39. J.L. Gu, Y. Shao, H.T. Bu, J.L. Jia and K.F. Yao: An abnormal correlation between electron work function and corrosion resistance in Ti-Zr-Be-(Ni/Fe) metallic glasses *Corros Sci.* **165**, (2020).
- 40. C.D. Taylor and H.B. Ke: Investigations of the intrinsic corrosion and hydrogen susceptibility of metals and alloys using density functional theory *Corros Rev.* **39**(3), 177 (2021).
- 41. B.L. Lu, G.Q. Chen, W.L. Zhou and H. Su: A density functional theory study on influence of 3d alloying elements on electrochemical properties of cobalt-base alloys *Comp Mater Sci.* **68**, 206 (2013).
- 42. A. Sundar, G.L. Chen and L. Qi: Substitutional adsorptions of chloride at grain boundary sites on hydroxylated alumina surfaces initialize localized corrosion *Npj Mat Degrad.* **5**(1), (2021).
- 43. Y.H. Zhao, C.Y. Luo, X.K. Xi, D.Q. Zhao, M.X. Pan and W.H. Wang: Synthesis and elastic properties of amorphous steels with high Fe content *Intermetallics*. **14**(8), 1107 (2006).
- 44. M.S.A. Karunaratne, S. Kyaw, A. Jones, R. Morrell and R.C. Thomson: Modelling the coefficient of thermal expansion in Ni-based superalloys and bond coatings *Journal of Materials Science*. **51**(9), 4213 (2016).
- 45. Z. Wang, Q. Wu, W. Zhou, F. He, C. Yu, D. Lin, J. Wang and C.T. Liu: Quantitative determination of the lattice constant in high entropy alloys *Scripta Materialia*. **162**, 468 (2019).
- 46. S. Qiu, X.-C. Zhang, J. Zhou, S. Cao, H. Yu, Q.-M. Hu and Z. Sun: Influence of lattice distortion on stacking fault energies of CoCrFeNi and Al-CoCrFeNi high entropy alloys *Journal of Alloys and Compounds.* **846**, 156321 (2020).
- 47. Y.-F. Kao, T.-J. Chen, S.-K. Chen and J.-W. Yeh: Microstructure and mechanical property of as-cast, -homogenized, and -deformed AlxCoCrFeNi (0≤x≤2) high-entropy alloys *Journal of Alloys and Compounds*. **488**(1), 57 (2009).

- 48. X.F. Wang, Y. Zhang, Y. Qiao and G.L. Chen: Novel microstructure and properties of multicomponent CoCrCuFeNiTix alloys *Intermetallics*. **15**(3), 357 (2007).
- 49. T.-T. Zuo, S.-B. Ren, P.K. Liaw and Y. Zhang: Processing effects on the magnetic and mechanical properties of FeCoNiAl0.2Si0.2 high entropy alloy *International Journal of Minerals, Metallurgy, and Materials.* **20**(6), 549 (2013).
- 50. K. Zhang and Z. Fu: Effects of annealing treatment on properties of CoCrFeNiTiAlx multi-component alloys *Intermetallics.* **28**, 34 (2012).
- 51. S. Singh, N. Wanderka, K. Kiefer, K. Siemensmeyer and J. Banhart: Effect of decomposition of the Cr–Fe–Co rich phase of AlCoCrCuFeNi high entropy alloy on magnetic properties *Ultramicroscopy.* **111**(6), 619 (2011).
- 52. M.S. Lucas, L. Mauger, J.A. Muñoz, Y. Xiao, A.O. Sheets, S.L. Semiatin, J. Horwath and Z. Turgut: Magnetic and vibrational properties of high-entropy alloys *Journal of Applied Physics*. **109**(7), 07E307 (2011).
- P. Koželj, S. Vrtnik, A. Jelen, S. Jazbec, Z. Jagličić, S. Maiti, M. Feuerbacher, W. Steurer and J. Dolinšek: Discovery of a Superconducting High-Entropy Alloy *Physical Review Letters*. 113(10), (2014).
- 54. H. Guan, S. Huang, J. Ding, F. Tian, Q. Xu and J. Zhao: Chemical environment and magnetic moment effects on point defect formations in CoCrNi-based concentrated solid-solution alloys *Acta Materialia*. **187**, 122 (2020).
- 55. S. Lu, H. Zhang, Q.M. Hu, M.P. Punkkinen, B. Johansson and L. Vitos: Magnetic effect on the interfacial energy of the Ni(1 1 1)/Cr(1 1 0) interface *J Phys Condens Matter.* **26**(35), 355001 (2014).
- 56. M.-H. Tsai: Physical Properties of High Entropy Alloys Entropy. 15(12), 5338 (2013).
- 57. Y. Zhang, T. Zuo, Y. Cheng and P.K. Liaw: High-entropy Alloys with High Saturation Magnetization, Electrical Resistivity and Malleability *Scientific Reports.* **3**(1), (2013).
- 58. C. Li, J. Yin, K. Odbadrakh, B.C. Sales, S.J. Zinkle, G.M. Stocks and B.D. Wirth: First principle study of magnetism and vacancy energetics in a near equimolar NiFeMnCr high entropy alloy *Journal of Applied Physics.* **125**(15), 155103 (2019).
- 59. X. Sun, H. Zhang, S. Lu, X. Ding, Y. Wang and L. Vitos: Phase selection rule for Al-doped CrMnFeCoNi high-entropy alloys from first-principles *Acta Materialia*. **140**, 366 (2017).
- 60. V. Wang, N. Xu, J.-C. Liu, G. Tang and W.-T. Geng: VASPKIT: A user-friendly interface facilitating high-throughput computing and analysis using VASP code *Computer Physics Communications.* **267**, 108033 (2021).
- 61. G. Laplanche, P. Gadaud, C. Bärsch, K. Demtröder, C. Reinhart, J. Schreuer and E.P. George: Elastic moduli and thermal expansion coefficients of medium-entropy subsystems of the CrMnFeCoNi high-entropy alloy *Journal of Alloys and Compounds.* **746**, 244 (2018).
- 62. S.F. Pugh: XCII. Relations between the elastic moduli and the plastic properties of polycrystalline pure metals *The London, Edinburgh, and Dublin Philosophical Magazine and Journal of Science.* **45**(367), 823 (1954).
- 63. S.L. Shang, A. Saengdeejing, Z.G. Mei, D.E. Kim, H. Zhang, S. Ganeshan, Y. Wang and Z.K. Liu: First-principles calculations of pure elements: Equations of state and elastic stiffness constants *Computational Materials Science*. **48**(4), 813 (2010).
- 64. H. Niu, X.-Q. Chen, P. Liu, W. Xing, X. Cheng, D. Li and Y. Li: Extra-electron induced covalent strengthening and generalization of intrinsic ductile-to-brittle criterion *Scientific Reports*. **2**(1), (2012).
- 65. H. Lu, Z.R. Liu, X.G. Yan, D.Y. Li, L. Parent and H. Tian: Electron work function-a promising guiding parameter for material design *Sci Rep-Uk.* **6**, (2016).
- 66. Z. Wang, D.Y. Li, Y.-Y. Yao, Y.-L. Kuo and C.-H. Hsueh: Wettability, electron work function and corrosion behavior of CoCrFeMnNi high entropy alloy films *Surface and Coatings Technology*. **400**, 126222 (2020).
- 67. X.C. Huang, H. Lu and D.Y. Li: Understanding the corrosion behavior of isomorphous Cu–Ni alloy from its electron work function *Materials Chemistry and Physics*. **173**, 238 (2016).
- 68. P. Marcus and V. Maurice: Atomic level characterization in corrosion studies *Philosophical Transactions of the Royal Society A: Mathematical, Physical and Engineering Sciences.* 375(2098), 20160414 (2017).
- 69. L. Guo, C. Qi, X. Zheng, R. Zhang, X. Shen and S. Kaya: Toward understanding the adsorption mechanism of large size organic corrosion inhibitors on an Fe(110) surface using the DFTB method *RSC Advances*. 7(46), 29042 (2017).
- 70. J.K. Norskov, F. Abild-Pedersen, F. Studt and T. Bligaard: Density functional theory in surface chemistry and catalysis *P Natl Acad Sci USA*. **108**(3), 937 (2011).

- 71. C.M. Tian, M. Jiang, D. Tang, L. Qiao, H.Y. Xiao, F.E. Oropeza, J.P. Hofmann, E.J.M. Hensen, A. Tadich, W. Li, D.C. Qi and K.H.L. Zhang: Elucidating the electronic structure of CuWO4 thin films for enhanced photoelectrochemical water splitting *J Mater Chem A.* 7(19), 11895 (2019).
- 72. W.B. Wang, K.W. Wang, Z.Y. Zhang, J. Chen, T.Y. Mou, F.M. Michel, H.L. Xin and W.J. Cai: Ultrahigh tribocorrosion resistance of metals enabled by nano-layering *Acta Mater.* **206**, (2021).
- 73. Y. Zhou, H.H. Xiong, Y.H. Yin and S.W. Zhong: First principles study of surface properties and oxygen adsorption on the surface of Al3Ti intermetallic alloys *Rsc Adv.* **9**(4), 1752 (2019).
- 74. F. Tang, L. Wang, M. Dessie Walle, A. Mustapha and Y.-N. Liu: An alloy chemistry strategy to tailoring the d-band center of Ni by Cu for efficient and selective catalytic hydrogenation of furfural *Journal of Catalysis*. **383**, 172 (2020).
- 75. Y. Chang, Y. Cheng, Y.L. Feng, K. Li, H. Jian and H.Y. Zhang: Upshift of the d Band Center toward the Fermi Level for Promoting Silver Ion Release, Bacteria Inactivation, and Wound Healing of Alloy Silver Nanoparticles *Acs Appl Mater Inter.* **11**(13), 12224 (2019).
- 76. J.H.E. Jeffes: Ellingham Diagrams, in Encyclopedia of Materials: Science and Technology, edited by K. H. J. Buschow, R. W. Cahn, M. C. Flemings, B. Ilschner, E. J. Kramer, S. Mahajan and P. Veyssière (Elsevier, City, 2001), pp. 2751.
- 77. L.T. Wang, D. Mercier, S. Zanna, A. Seyeux, M. Laurent-Brocq, L. Perriere, I. Guillot and P. Marcus: Study of the surface oxides and corrosion behaviour of an equiatomic CoCrFeMnNi high entropy alloy by XPS and ToF-SIMS *Corros Sci.* **167**, (2020).
- 78. C.B. Nascimento, U. Donatus, C.T. Ríos and R.A. Antunes: Electronic properties of the passive films formed on CoCrFeNi and CoCrFeNiAl high entropy alloys in sodium chloride solution *Journal of Materials Research and Technology*. **9**(6), 13879 (2020).
- 79. G. Kresse and J. Furthmüller: Efficient iterative schemes for ab initio total-energy calculations using a plane-wave basis set *Physical Review B*. **54**(16), 11169 (1996).
- 80. G. Kresse and D. Joubert: From ultrasoft pseudopotentials to the projector augmented-wave method *Physical Review B.* **59**(3), 1758 (1999).
- 81. J.P. Perdew, K. Burke and M. Ernzerhof: Generalized Gradient Approximation Made Simple *Physical Review Letters*. 77(18), 3865 (1996).
- 82. A. Zunger, S.H. Wei, L.G. Ferreira and J.E. Bernard: Special quasirandom structures *Physical Review Letters*. **65**(3), 353 (1990).
- 83. A. van de Walle, P. Tiwary, M. de Jong, D.L. Olmsted, M. Asta, A. Dick, D. Shin, Y. Wang, L.Q. Chen and Z.K. Liu: Efficient stochastic generation of special quasirandom structures *Calphad.* **42**, 13 (2013).
- 84. Y. Le Page and P. Saxe: Symmetry-general least-squares extraction of elastic coefficients from ab initio total energy calculations *Physical Review B.* **63**(17), 174103 (2001).
- 85. F. Tasnádi, M. Odén and I.A. Abrikosov: Ab initioelastic tensor of cubic Ti0.5Al0.5N alloys: Dependence of elastic constants on size and shape of the supercell model and their convergence *Physical Review B.* **85**(14), (2012).
- 86. G. Kim, H. Diao, C. Lee, A.T. Samaei, T. Phan, M. de Jong, K. An, D. Ma, P.K. Liaw and W. Chen: First-principles and machine learning predictions of elasticity in severely lattice-distorted high-entropy alloys with experimental validation *Acta Materialia*. **181**, 124 (2019).
- 87. F. Mouhat and F.-X. Coudert: Necessary and sufficient elastic stability conditions in various crystal systems *Physical Review B.* **90**(22), (2014).
- 88. W. Voigt: Lehrbuch der Kristallphysik (BG Teubner Leipzig und Berlin) 980 S Reproduced 1966 Spring Fachmedien Wiesbaden GmbH. (1928).
- 89. A. Reuss: Berechnung der Fließgrenze von Mischkristallen auf Grund der Plastizitätsbedingung für Einkristalle ZAMM Journal of Applied Mathematics and Mechanics / Zeitschrift für Angewandte Mathematik und Mechanik. 9(1), 49 (1929).
- 90. R. Hill: The Elastic Behaviour of a Crystalline Aggregate *Proceedings of the Physical Society*. *Section A.* **65**(5), 349 (1952).
- 91. H. Lu, Z. Liu, X. Yan, D. Li, L. Parent and H. Tian: Electron work function—a promising guiding parameter for material design *Scientific Reports.* **6**(1), 24366 (2016).
- 92. T.Y. Ma, R. Jacobs, J. Booske and D. Morgan: Understanding the interplay of surface structure and work function in oxides: A case study on SrTiO3 (vol 8, 071110, 2020) *Apl Mater.* **9**(1), (2021).
- 93. O.T. Hofmann, J.C. Deinert, Y. Xu, P. Rinke, J. Stahler, M. Wolf and M. Scheffler: Large work function reduction by adsorption of a molecule with a negative electron affinity: Pyridine on ZnO(10(1)over-bar0) *J Chem Phys.* **139**(17), (2013).

# **Tables and Figures**

**Table 1**. Summary of calculated lattice constant (d), bulk modulus (B), Young's modulus (E), shear modulus (G), and electron work function (EWF) for all CoCrFeNi alloys.

Sample	Composition (at.%)	d (Å)	B (GPa)	E (GPa)	G (GPa)	B/G	EWF (eV)	
Cr16	Co <sub>28</sub> Cr <sub>16</sub> Fe <sub>28</sub> Ni <sub>28</sub>	3.56	160.510	216.504	84.891	1.891	(100) plane	4.363
							(110) plane	4.164
							(111) plane	4.821
Cr25	Co <sub>25</sub> Cr <sub>25</sub> Fe <sub>25</sub> Ni <sub>25</sub>	3.54	157.087	226.211	89.767	1.750	(100) plane	4.552
							(110) plane	4.173
							(111) plane	4.849
Cr34	Co <sub>22</sub> Cr <sub>34</sub> Fe <sub>22</sub> Ni <sub>22</sub>	3.53	181.804	224.539	86.751	2.096	(100) plane	4.407
							(110) plane	4.181
							(111) plane	4.815

**Table 2.** Summary of calculated mechanical properties of Cr25 alloy (as defined in Table 1) from this work, prior DFT reports  $^{26}$  and experiments  $^{61}$ . Note results in ref.  $^{61}$  were measured at room temperature. DFT w/o spin<sup>(a)</sup> use k-points  $4\times4\times4$  and energy cutoff of 400 eV, and DFT w/o spin<sup>(b)</sup> use k-points  $7\times7\times7$  and energy cutoff of 450 eV.

Methods	E (GPa)	G (GPa)	B (GPa)	B/G	v
DFT w/o spin (this work) <sup>(a)</sup>	387	166	193	1.16	0.17
DFT w/o spin (this work) <sup>(b)</sup>	247	94	207	2.18	0.30
DFT w/ spin (this work)	226	90	157	1.75	0.26
Expt. (ref <sup>61</sup> )	214	86	142	1.65	0.25
DFT (ref <sup>26</sup> )	298	118	202	1.71	0.26

**Table 3.** Comparison of material properties from DFT vs. rule of mixture (ROM) calculations where a parameter p is calculated by summing the parameter  $p_i$  of each constituent (i) times its weight fraction  $(w_i)$  as  $p = \sum_{i=1}^n w_i p_i$ .

Sample	υ		B	/G	(110) EWF (eV)		
Sample	ROM	DFT	ROM	DFT	ROM	DFT	
Cr16	0.286	0.275	4.69	4.164	2.15	1.89	
Cr25	0.276	0.260	4.66	4.173	2.06	1.75	
Cr34	0.267	0.294	4.63	4.181	1.97	2.10	

Table 4. D-band center of Co, Cr, Fe, and Ni element in Cr16, Cr25 and Cr34 alloys.

Sample Element	Cr16	Cr25	Cr34
Со	-1.29 eV	-1.34 eV	-1.42 eV
Cr	-0.08 eV	-0.10 eV	-0.39 eV
Fe	-1.02 eV	-1.14 eV	-1.23 eV
Ni	-1.53 eV	-1.47 eV	-1.58 eV

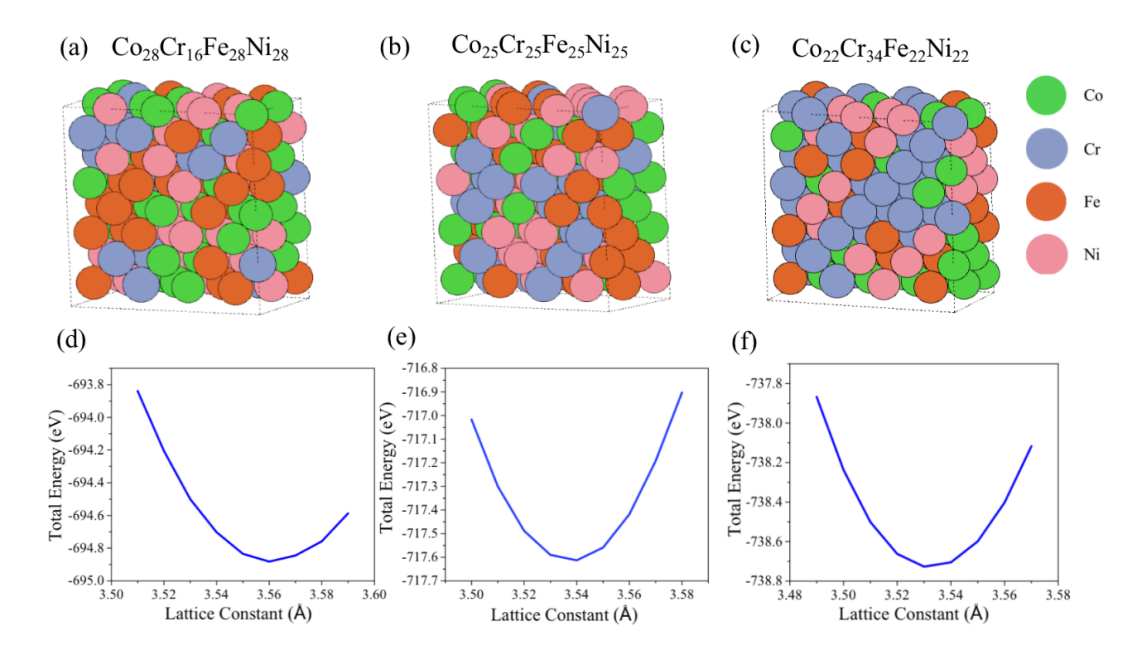


**Figure 1**. (a-c) SQS model structure and (d-f) calculated lattice constant for (a) Cr16, (b) Cr25, and (c) Cr34 alloys.

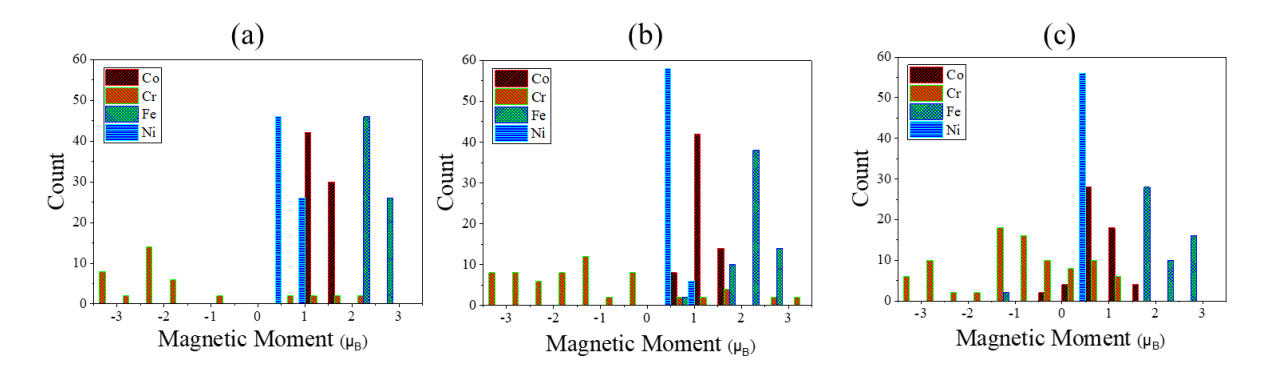
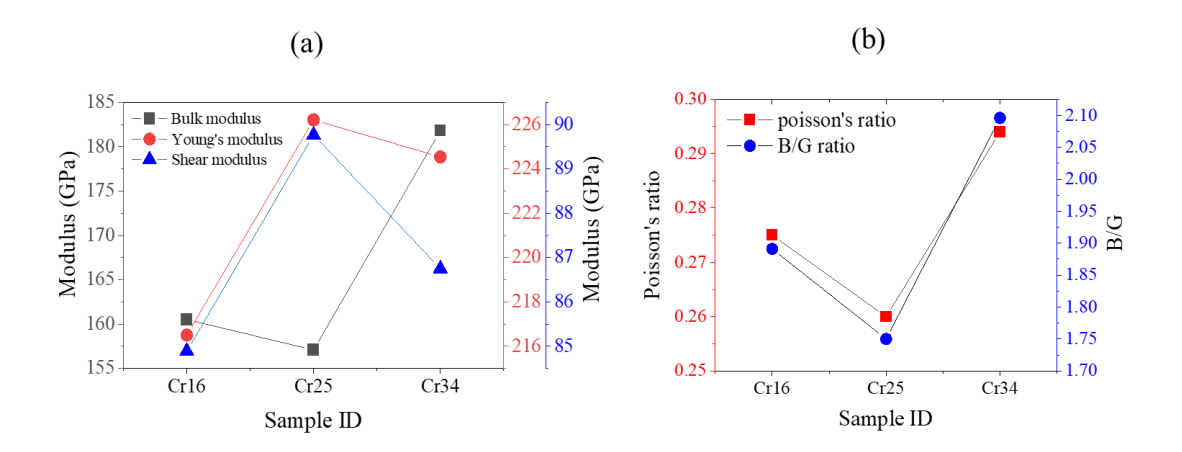
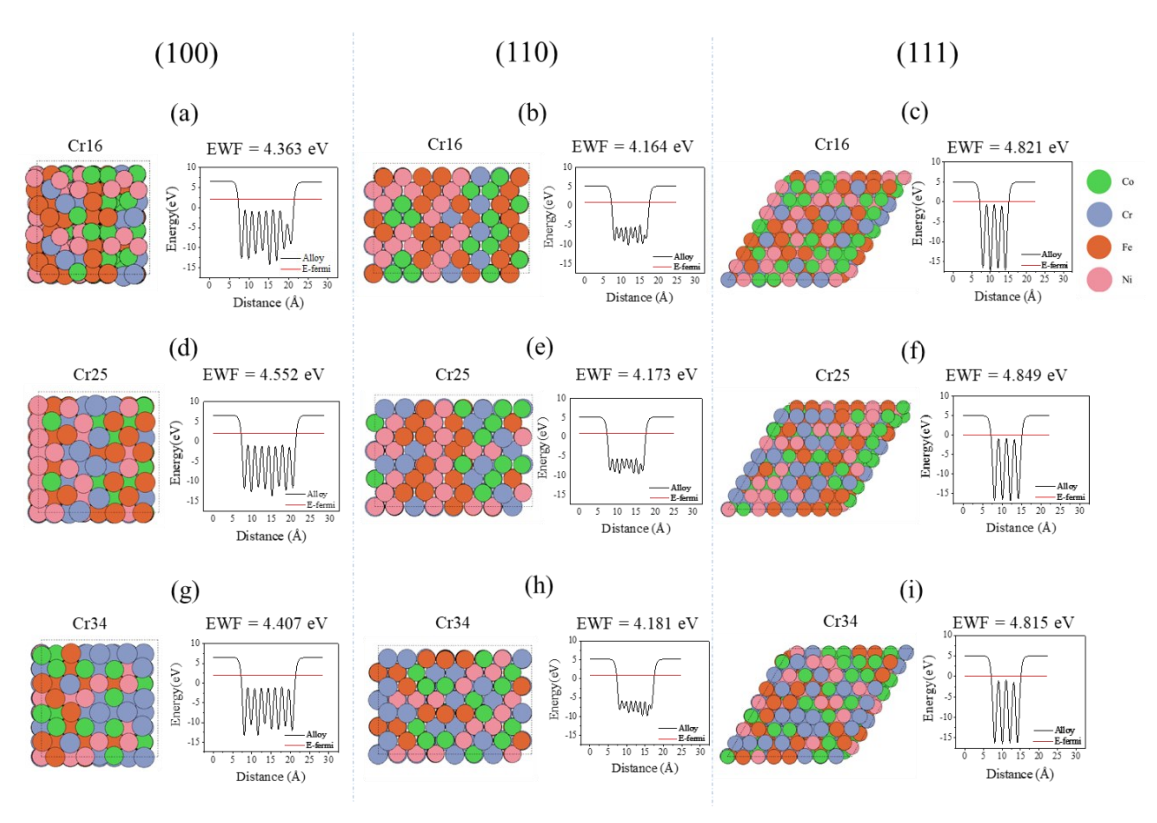


Figure 2. Histogram of magnetic moment of (a) Cr16, (b) Cr25 and (c) Cr34 alloys for the (110) orintation model.



**Figure 3**. Summary of calculated elastic properties for Cr16, Cr25 and Cr24 alloys, (a) bulk modulus, Young's modulus and shear modulus, (b) Poisson's ratio and B/G ratio.



**Figure 4**. Summary of calculated EWF of (100), (110) and (111) surfaces of (a-c) Cr16, (d-f) Cr25, and (g-i) Cr34 alloys.

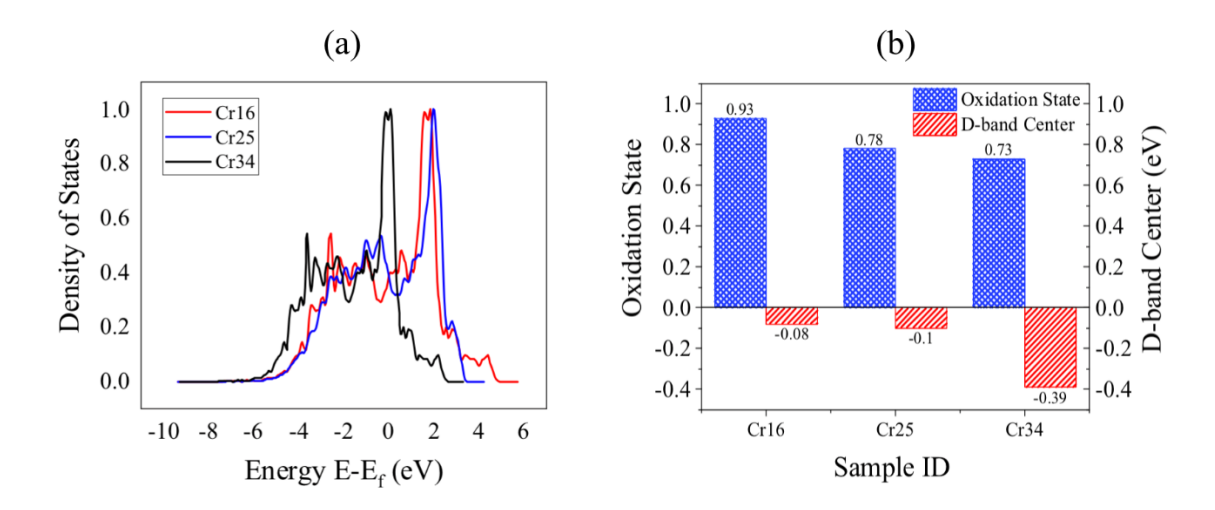


**Figure 5.** Calculated electrical properties on the (110) surface of all alloys. (a) D-band density of states of Cr, and (b) oxidation state and Cr d-band center from surface atoms of all alloys.

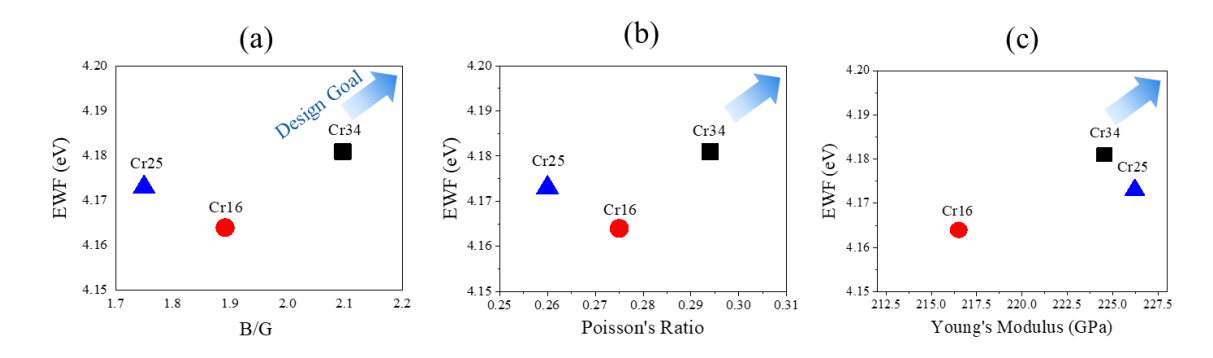


**Figure 6**. Summary of calculated (110) surface EWF vs. (a) B/G ratio, (b) Poisson's ratio, and (c) Young's modulus of all alloys.

# **Supplemental Materials**

**Table S1**. Calculated average magnetic moment and mechanical properties of Cr16, Cr 25, and Cr 34 alloys.

Sample	Со (µв)	Cr (µ <sub>B</sub> )	Fe (μ <sub>B</sub> )	Ni (μ <sub>B</sub> )	Alloy (μ <sub>B</sub> )	C <sub>11</sub>	C <sub>12</sub>	C44
						(GPa)	(GPa)	(GPa)
Cr16	1.43	-1.53	2.48	0.45	0.99	225.836	127.944	122.993
Cr25	1.28	-1.11	2.24	0.31	0.67	223.602	124.144	134.136
Cr34	0.89	-0.82	2.06	0.20	0.41	241.750	152.461	135.912

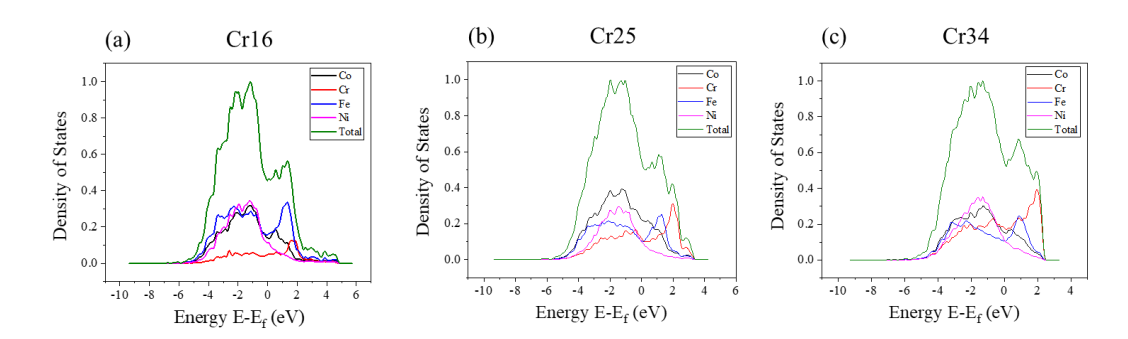
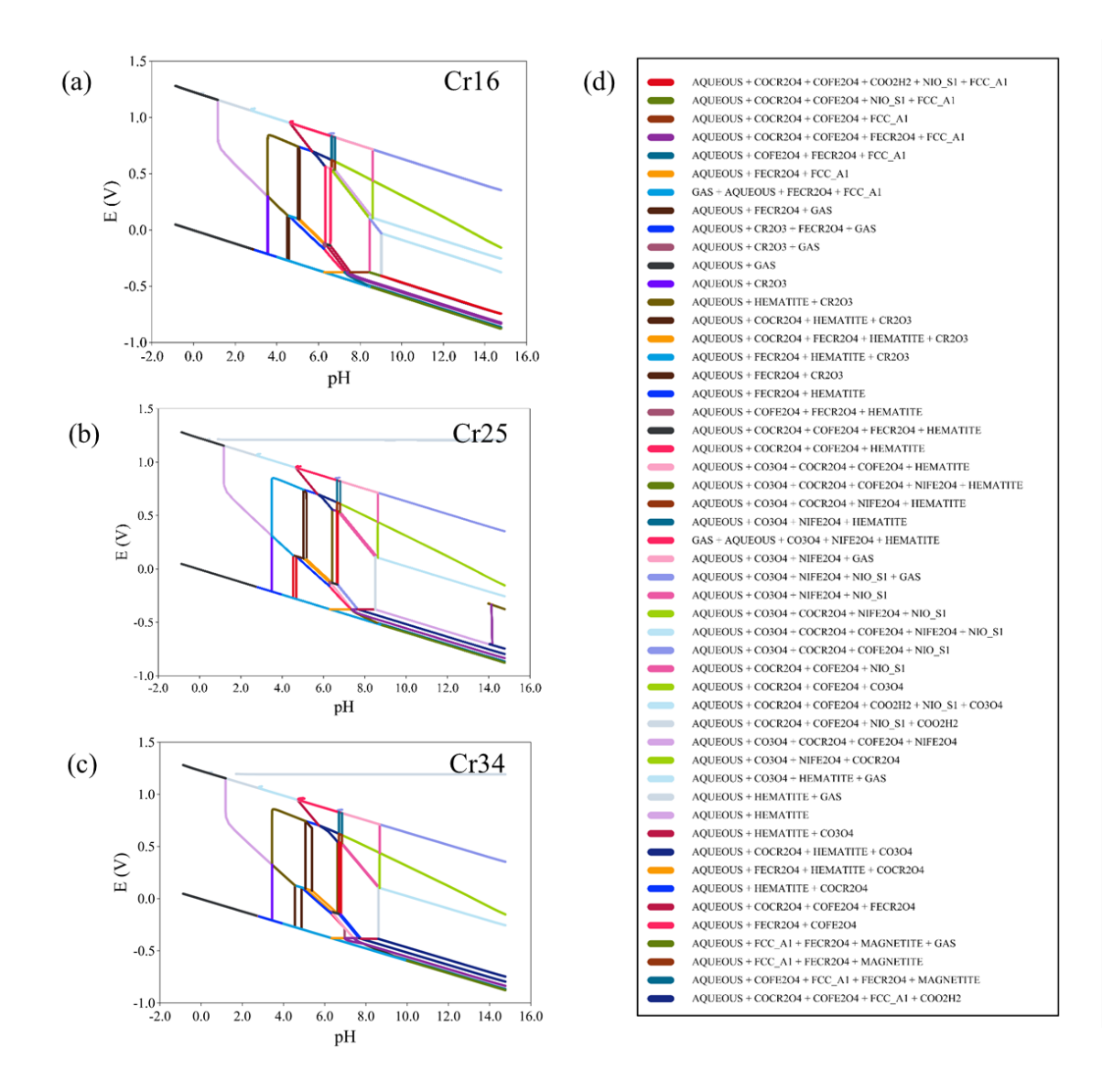


Figure S1. Total and partial DOS of (a) Cr16, (b) Cr25 and (c) Cr34 alloys of (110) surfaces.



**Figure S2**. Calcualted Pourbaix diagram of (a) Cr16, (b) Cr25, and (c) Cr34, where the predicted equilibrium phases are shown in the legend in (d). The calculations were performed using Thermo-calc software version 2022a using the TCFE12 database.